Journal of Computational Mathematics
Vol.35, No.3, 2017, 363–380.

http://www.global-sci.org/jcm
doi:10.4208/jcm.1702-m2016-0630

A PARALLEL ALGORITHM FOR THE SOLUTION OF LARGE-SCALE NONCONFORMING FLUID-STRUCTURE INTERACTION PROBLEMS IN HEMODYNAMICS *

Davide Forti, Alfio Quarteroni and Simone Deparis
MATH-CMCS, École Polytechnique Fédérale de Lausanne,
Station 8, CH-1015 Lausanne, Switzerland
Email: davide.forti@epfl.ch, alfio.quarteroni@epfl.ch, simone.deparis@epfl.ch

Abstract

In this work we address the numerical solution of large scale fluid-structure interaction problems when nonconforming grids and/or nonconforming finite elements discretizations are used at the interface separating the fluid and structure physical domains. To deal with nonconforming fluid-structure discretizations we use the INTERNODES method (INTERpolation for NOnconforming DEcompositionS) formerly introduced in [6] for the solution of elliptic PDEs on nonconforming domain decomposition. To cope with the high computational complexity of the three dimensional FSI problem obtained after spatial and temporal discretization, we use the block parallel preconditioner FaCSI [7]. A numerical investigation of the accuracy properties of INTERNODES applied to the nonconforming FSI problem is carried out for the simulation of the pressure wave propagation in a straight elastic cylinder. Finally, we study the scalability performance of the FaCSI preconditioner in the nonconforming case by solving a large-scale nonconforming FSI problem in a patient-specific arterial bypass.

Mathematics subject classification: 74F10, 65M55.
Key words: Fluid-Structure Interaction, Domain Decomposition, Nonconforming discretizations, INTERNODES, Biomechanics, Parallel Preconditioners, High Performance Computing.

1. Introduction

Fluid-Structure Interaction (FSI) problems are systems of partial differential equations that couple together flow models (typically described by Navier-Stokes equations) and structural models (typically expressed by the nonlinear elastodynamics equations) through an interface where both dynamics and kinematics coupling conditions are fulfilled [4, 5]. In this work we are interested in the numerical solution by finite elements of FSI problems when nonconforming discretizations are used for the fluid and the structure computational domains. Typically, solution algorithms for fluid-structure interaction problems are derived assuming that conforming fluid-structure discretizations are used at the fluid-structure interface. In such cases, the enforcement of the coupling conditions is straightforward. However, due to the different resolution requirements in the fluid and structure physical domains, as well as the presence of complex interface geometries that do not match exactly make the use of matching fluid and structure meshes problematic. In these situations, it is more natural to deal with discretizations that

* Received May 9, 2016 / Revised version received August 29, 2016 / Accepted February 21, 2017 / Published online April 25, 2017 /

are nonconforming, provided however that the coupling conditions at the interface are properly enforced.

In this work, to deal with nonconforming discretizations at the discrete fluid-structure interface we use INTERNODES (INTERpolation for NOnconforming DEcompositionS), an interpolation based method that has been proposed in [6] for the numerical solution of elliptic partial differential equations on nonconforming domain decompositions. INTERNODES is in fact an alternative to the mortar element method, introduced in the context of nonoverlapping domain decomposition [11, 12]. The mortar element method has already been used in the context of nonconforming fluid-structure interaction problems, see e.g. [13–17]. In [18] a dual mortar method was used with discrete Lagrange multipliers that are constructed on a biorthogonality relation with the primal shape functions at the fluid-structure interface. Besides the mortar element method, other coupling strategies have been proposed in the framework of partitioned solution schemes for fluid-structure interaction problems, see [19–21] and references therein.

In our spatial simulation settings we allow the fluid computational grid and/or the fluid finite element discretization to be nonconforming with the structural one at the interface. Even worse, the two interfaces could be geometrically nonconforming, a situation that arises when the two subdomains are triangulated independently. In such nonconforming cases, the kinematic and dynamic coupling conditions between the fluid and structure domains are imposed at the interface by the INTERNODES method. One distinguishing feature of INTERNODES is that it makes use of two interpolants to carry out the transfer of information across the interface: one from master to slave and another one from slave to master. In our algorithm the structural domain is the master while the fluid domain is the slave. Then, we build up two Radial Basis Function (RBF) inter-grid operators, one Π_{sf} from master to slave, and another Π_{fs} from slave to master. We enforce the kinematic condition by equating the fluid velocity at the interface as the image through Π_{fs} of the temporal derivative of the structural displacement. The dynamic interface condition is instead enforced via a variational method wherein the strong form of the structural normal component of the Cauchy stresses is obtained as the image through Π_{sf} of the strong form of the normal component of the fluid stresses (the traction).

We solve the resulting nonlinear FSI problem using a monolithic scheme in which all the nonlinearities are treated implicitly. To cope with the high computational complexity of the three dimensional FSI problem, we use FaCSI, a block parallel preconditioner proposed in [7] for the coupled linearized FSI system obtained after space and time discretization. FaCSI exploits the factorized form of the FSI Jacobian matrix, a static condensation procedure to formally eliminate the interface degrees of freedom of the fluid equations, and the SIMPLE preconditioner for the matrix block generated by the space-time discretization of the unsteady Navier-Stokes equations.

As a first numerical example, we solve the fluid-structure interaction problem on a cylindrical geometry. We assess the accuracy of the INTERNODES method by performing a mesh convergence study using both nonconforming meshes and polynomial interpolation at the fluid-structure interface. Furthermore, we investigate the strong and weak scalability properties of FaCSI using nonconforming discretizations. We compare the results obtained with those of the fully conforming case. We show that FaCSI yields almost the same scalability performance regardless the use of conforming or nonconforming discretizations between the fluid and the structure at their interface. As a second example, we address a large-scale simulation of blood flow in a patient-specific arterial bypass: we show that the results obtained using nonconforming discretizations (fluid velocity, wall shear stress and solid displacement) are in good

agreement with those reported in [7] where conforming discretizations at the fluid-structure interface were adopted.

The remainder of the paper is organized as follows. In Section 2 we describe the FSI model adopted in this work. Then, in Section 3, after introducing the spatial and temporal discretizations of the problem, we describe how the INTERNODES method is used for the coupling of nonconforming fluid-structure interface discretizations. In Section 4 we describe the monolithic solution algorithm, as well as the parallel preconditioner FaCSI, used to solve the nonlinear FSI problem. In Section 5.1 we carry out a mesh convergence study by solving the FSI in a straight flexible cylinder. Finally, in Section 5.3, we address the simulation of blood flow in a patient-specific geometry of a femoropopliteal bypass. Conclusions are drawn in Section 6.

2. Fluid-Structure Interaction Model

In this section we describe the fluid-structure interaction model that we have adopted. Let $\hat{\Omega}^f$ and $\hat{\Omega}^s$ be the fluid and solid domains, respectively, in their reference configuration. We denote by $\hat{\Gamma} = \partial\hat{\Omega}^f \cap \partial\hat{\Omega}^s$ the fluid-structure interface on the reference configuration. At any time $t > 0$, the current fluid domain configuration Ω_t^f can be retrieved from $\hat{\Omega}^f$ by the Arbitrary Lagrangian Eulerian (ALE) mapping

$$\begin{aligned} \mathcal{A}_t : \quad & \hat{\Omega}^f \to \Omega_t^f \\ & \mathbf{X} \mapsto \mathcal{A}_t(\mathbf{X}) = \mathbf{X} + \hat{\mathbf{d}}_f(\mathbf{X}), \end{aligned} \tag{2.1}$$

where $\hat{\mathbf{d}}_f$ represents the displacement of the fluid domain. The use of the ALE formulation allows an arbitrary reconstruction of the volumetric computational grid of Ω_t^f from the one of the domain boundary $\partial\Omega_t^f$. For the sake of computation, this reconstruction is directly operated on the reference configuration by means of a harmonic extension of the structure displacement $\hat{\mathbf{d}}_s$ at the fluid-structure interface $\hat{\Gamma}$ to the interior of the reference fluid domain $\hat{\Omega}^f$, i.e.,

$$\begin{cases} -\Delta\hat{\mathbf{d}}_f = \mathbf{0} & \text{in } \hat{\Omega}^f, \\ \hat{\mathbf{d}}_f = \hat{\mathbf{d}}_s & \text{on } \hat{\Gamma}. \end{cases} \tag{2.2}$$

As the solid displacement $\hat{\mathbf{d}}_s$ changes in time, Eq. (2.2) allows to define the current fluid domain configuration $\Omega_t^f = \mathcal{A}_t(\hat{\Omega}^f)$ thanks to the ALE map parametrization (2.1).

In our FSI model, the fluid dynamics is governed by the incompressible Navier-Stokes equations written in the ALE frame of reference [4, 5],

$$\begin{cases} \rho_f \left(\left.\dfrac{\partial \mathbf{u}}{\partial t}\right|_{\mathbf{X}} + ((\mathbf{u} - \mathbf{w}) \cdot \nabla)\mathbf{u} \right) - \nabla \cdot \boldsymbol{\sigma}_f(\mathbf{u}, p) = 0 & \text{in } \Omega_t^f \times (0, T], \\ \nabla \cdot \mathbf{u} = 0 & \text{in } \Omega_t^f \times (0, T]. \end{cases} \tag{2.3}$$

In (2.3), $\left.\frac{\partial}{\partial t}\right|_{\mathbf{X}} = \frac{\partial}{\partial t} + \mathbf{w} \cdot \nabla$ is the ALE derivative, $(0, T]$ is the time interval, ρ_f is the fluid density, $\mathbf{u}$ and p are the fluid velocity and pressure, respectively, and $\boldsymbol{\sigma}_f(\mathbf{u}, p) = 2\mu_f\boldsymbol{\epsilon}(\mathbf{u}) - p\mathbf{I}$ is the Cauchy stress tensor ($\mathbf{I}$ is the identity matrix) for a Newtonian fluid. We denoted by $\boldsymbol{\epsilon}(\mathbf{u}) = \frac{1}{2}\left(\nabla\mathbf{u} + (\nabla\mathbf{u})^T\right)$ the strain rate tensor and by μ_f the dynamic viscosity of the fluid. Furthermore, $\mathbf{w}$ is the fluid mesh velocity,

$$\mathbf{w} = \left.\frac{\partial \hat{\mathbf{d}}_f}{\partial t}\right|_{\mathbf{X}}.$$

DOI https://doi.org/10.4208/jcm.1702-m2016-0630 | Generated on 2024-12-19 07:04:00

We formulate the structure problem in a Lagrangian frame of reference. The conservation of momentum for the structure reads

$$\rho_s \frac{\partial^2 \hat{\mathbf{d}}_s}{\partial t^2} - \nabla \cdot (\mathbf{FS}) = 0 \quad \text{in } \hat{\Omega}^s \times (0,T], \tag{2.4}$$

where ρ_s is the density of the structure and $\mathbf{FS}$ are the first Piola-Kirchhoff stresses.

The coupling between the geometry, fluid and structure subproblems is expressed by

$$\hat{\mathbf{d}}_f = \hat{\mathbf{d}}_s, \tag{2.5}$$

$$\frac{\partial \hat{\mathbf{d}}_s}{\partial t} = \mathbf{u} \circ \mathcal{A}_t, \tag{2.6}$$

$$(\det[\mathbf{F}])^{-1} \mathbf{F}^{-T} \boldsymbol{\sigma}_f \circ \mathcal{A}_t \, \hat{\mathbf{n}}_f + (\mathbf{FS})\, \hat{\mathbf{n}}_s = 0, \tag{2.7}$$

where (2.5) expresses the geometric adherence, (2.6) the continuity of the velocities (kinematic condition) and (2.7) the continuity of the stresses (dynamic condition) on $\hat{\Gamma}$.

The resulting system of equations describing the FSI problem is nonlinear due to the moving fluid domain, the convective term in the fluid momentum equation, and the possible nonlinearity of the structural material model.

3. INTERNODES for Nonconforming Fluid-Structure Interaction Problems

We approximate the time derivative in the fluid momentum equation by means of second order implicit Backward Differentiation Formulas:

$$\frac{\partial \mathbf{u}}{\partial t}(t^{n+1})\bigg|_{\hat{\mathbf{x}}} \approx \frac{3\mathbf{u}^{n+1} - 4\mathbf{u}^n + \mathbf{u}^{n-1}}{2\Delta t}, \tag{3.1}$$

where Δt is time step size.

The time discretization of the structural problem is carried out by the Newmark method

$$\frac{\partial^2 \hat{\mathbf{d}}_s}{\partial t^2}(t^{n+1}) \approx \frac{1}{\beta \Delta t^2} \hat{\mathbf{d}}_s^{n+1} - \frac{1}{\beta \Delta t^2}(\hat{\mathbf{d}}_s^n + \Delta t\, \dot{\hat{\mathbf{d}}}_s^n) - \frac{1-2\beta}{2\beta}\, \ddot{\hat{\mathbf{d}}}_s^n, \tag{3.2}$$

where:

$$\ddot{\hat{\mathbf{d}}}_s^n = \frac{1}{\beta \Delta t^2} \hat{\mathbf{d}}_s^n - \frac{1}{\beta \Delta t^2}(\hat{\mathbf{d}}_s^{n-1} + \Delta t\, \dot{\hat{\mathbf{d}}}_s^{n-1}) - \frac{1-2\beta}{2\beta}\, \ddot{\hat{\mathbf{d}}}_s^{n-1}, \tag{3.3}$$

$$\dot{\hat{\mathbf{d}}}_s^n = \dot{\hat{\mathbf{d}}}_s^{n-1} + \Delta t\, (\gamma\, \ddot{\hat{\mathbf{d}}}_s^n + (1-\gamma)\, \ddot{\hat{\mathbf{d}}}_s^{n-1}). \tag{3.4}$$

In space, we consider a Galerkin finite element discretization. In our spatial simulation settings we allow the fluid computational grid and/or the fluid finite element discretization to be nonconforming with the structural one at the interface, see Figure 3.1.

Even worse, the two interfaces could be geometrically nonconforming, a situation which may arise when the two subdomains are triangulated independently.

In this work, to deal with nonconforming fluid-structure interface discretizations we use INTERNODES (INTERpolation for NOnconforming DEcompositionS), formerly proposed in [6] for elliptic PDEs. As for the mortar element method, in INTERNODES we need to identify the master and the slave domains Ω_{slave} and Ω_{master}, respectively. One distinguishing feature

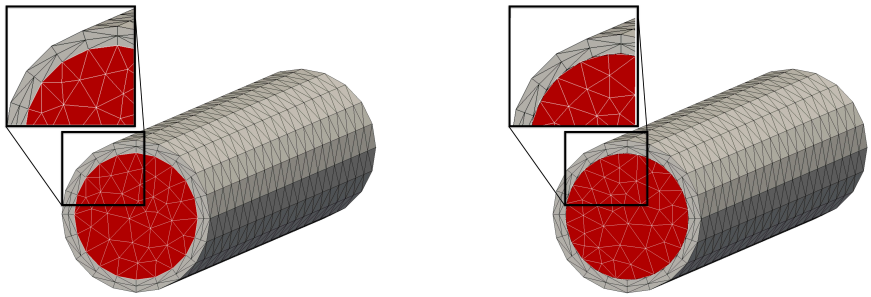

(a) Conforming meshes. (b) Non-conforming meshes.

Fig. 3.1. Conforming (left) and non-conforming (right) fluid–structure meshes.

of the INTERNODES method is that it makes use of two different interpolants[1)] to carry out the transfer of information across the interface: one from master to slave and another one from slave to master. One interpolant is used to ensure continuity of the velocity field, the other for ensuring the continuity of the dual variable (the traction). In this context, the dual variable (the normal component of the Cauchy stress tensor) in the slave domain is available in weak form: we first compute a strong representation of the dual variable from the slave side, interpolate it, transform the interpolated quantity back into weak form and eventually assign the function so obtained to the master side.

In our fluid-structure interaction problem, we assume the structure domain to be the master, $\hat{\Omega}^s \equiv \Omega_{master}$, while the fluid one represents the slave, $\Omega_t^f \equiv \Omega_{slave}$, then we build up two interpolation operators based on Rescaled-Localized Radial Basis Function (RL-RBF) [8]: one Π_{fs} from master to slave, and the other Π_{sf} from slave to master. We use interpolation operators based on Rescaled Localized Radial Basis Functions since they allow also to deal with slightly nonconforming geometries, i.e., those for which the fluid and structure discretizations do not exactly coincide (see, e.g., Figure 3.1(b)). At this stage, the kinematic condition is enforced by equating the fluid velocity at the interface as the image through Π_{fs} of the temporal derivative of the structural displacement. On the other hand, the dynamic interface condition is fulfilled via a variational method where the strong form of the structural normal stress is obtained as the image through Π_{sf} of the strong form of the fluid normal stress.

In particular, after spatial and temporal discretizations, the kinematic coupling condition at the fluid-structure interface reads:

$$\mathbf{u}^{n+1}|_{\Gamma^f} = R_{fs}\left(\frac{\gamma}{\beta\Delta t}\hat{\mathbf{d}}_s^{n+1}|_{\Gamma^s} + \mathbf{b}_c|_{\Gamma^s}\right), \tag{3.5}$$

where

$$\mathbf{b}_c|_{\Gamma^s} = \dot{\hat{\mathbf{d}}}_s^n|_{\Gamma^s} - \frac{\gamma}{\beta\Delta t}\left(\hat{\mathbf{d}}_s^n|_{\Gamma^s} + \Delta t\,\dot{\hat{\mathbf{d}}}_s^n|_{\Gamma^s}\right) - \Delta t\,\gamma\frac{1-2\beta}{2\beta}\,\ddot{\hat{\mathbf{d}}}_s^n|_{\Gamma^s} + \Delta t\,(1-\gamma)\,\ddot{\hat{\mathbf{d}}}_s^n|_{\Gamma^s} \tag{3.6}$$

and R_{fs} is the matrix associated with operator Π_{fs}. Eq. (3.5) represents the discrete form of the kinematic coupling condition in the nonconforming case.

We focus now on the coupling condition of the normal component of the stresses at the fluid-structure interface. Let us denote by $\boldsymbol{\lambda}_s^{n+1}$ the weak form of the normal component of

[1)] We remark that the interpolants characterizing the INTERNODES construction can be arbitrary.

the Cauchy stress (or normal traction) on Γ^s at time t^{n+1}, and by M_{Γ^s} and M_{Γ^f} the mass matrices associated to the structure and fluid sides of the interface, respectively. Thanks to INTERNODES the discrete form of the dynamic coupling condition reads:

$$\boldsymbol{\lambda}_s^{n+1} = M_{\Gamma^s} R_{sf} M_{\Gamma^f}^{-1} \boldsymbol{\lambda}_f^{n+1}. \tag{3.7}$$

In Eq. (3.7), we notice that $M_{\Gamma^f}^{-1}\boldsymbol{\lambda}_f^{n+1}$ is an approximation of the strong form of the normal component of the stresses on Γ^f; $R_{sf}(M_{\Gamma^f}^{-1}\boldsymbol{\lambda}_f^{n+1})$ is an interpolation of the normal component of the stresses on the side of Γ^s, still in strong form, and $M_{\Gamma^s}(\Pi_{sf} M_{\Gamma^f}^{-1}\boldsymbol{\lambda}_f^{n+1})$ is again in weak form but on Γ^s. Note that the order of magnitude of the entries of $\boldsymbol{\lambda}_f^{n+1}$ depend on the mesh size used to discretize Ω_t^f, that of the entries of $M_{\Gamma^s}(\Pi_{sf} M_{\Gamma^f}^{-1}\boldsymbol{\lambda}_f^{n+1})$ depend on the mesh size of $\hat{\Omega}^s$, while the order of magnitude of those of $M_{\Gamma^f}^{-1}\boldsymbol{\lambda}_f^{n+1}$ and $\Pi_{sf}(M_{\Gamma^f}^{-1}\boldsymbol{\lambda}_f^{n+1})$ are independent of the mesh sizes.

At each time step, the resulting nonlinear FSI system to be solved in the nonconforming case reads:

$$\begin{pmatrix} S(\hat{\mathbf{d}}_s^{n+1}) & + & 0 & + & 0 & - I_{\Gamma^s}^T M_{\Gamma^s} R_{sf} M_{\Gamma^f}^{-1} \boldsymbol{\lambda}_f^{n+1} \\ -R_{sf} I_{\Gamma^s} \hat{\mathbf{d}}^{n+1} & + G(\hat{\mathbf{d}}_f^{n+1}) & + & 0 & + & 0 \\ 0 & + & 0 & + F(\mathbf{u}^{n+1}, p^{n+1}, \hat{\mathbf{d}}_f^{n+1}) & + & I_{\Gamma^f}^T \boldsymbol{\lambda}_f^{n+1} \\ -\dfrac{\gamma}{\beta \Delta t} R_{fs} I_{\Gamma^s} \hat{\mathbf{d}}_s^{n+1} & + & 0 & + & I_{\Gamma^f} \mathbf{u}_f^{n+1} & + & 0 \end{pmatrix} = \begin{pmatrix} \mathbf{b}_s \\ 0 \\ \mathbf{b}_f \\ R_{fs}\mathbf{b}_c \end{pmatrix}. \tag{3.8}$$

The diagonal blocks on the left hand side of (3.8) account for the discretized solid, geometry and fluid problems while R_{fs} and R_{sf} are the matrices associated with the interpolation operators Π_{fs} and Π_{sf}, respectively. We remark that F is nonlinear due to the convective term and the fact that fluid domain moves. Finally, the matrices I_{Γ^f} and I_{Γ^s} are the restriction of fluid and structure vectors to the interface. See [9] for a complete derivation of (3.8).

4. Numerical Solution of the Nonlinear FSI Problem

We solve the nonlinear FSI problem (3.8) by the Newton method. The solution of (3.8) at time $t^n = n\,\Delta t$ is denoted by $\mathbf{X}^n = (\mathbf{d}_s^n, \mathbf{d}_f^n, (\mathbf{u}_f, p_f)^n, \boldsymbol{\lambda}_f^n)^T$. At each time step, we compute a sequence of approximations $\mathbf{X}_1^{n+1}$, $\mathbf{X}_2^{n+1}$, etc. until the numerical solution converges up to a prescribed tolerance. Starting from an approximation of $\mathbf{X}_k^{n+1}$, the generic $k+1$ iteration of the Newton method applied to (3.8) requires first to assemble the residual $\mathbf{R}_k^{n+1} = (\mathbf{r}_{\mathbf{d}_s,k}^{n+1}, \mathbf{r}_{\mathbf{d}_f,k}^{n+1}, r_{u,p_f,k}^{n+1}, \mathbf{r}_{\boldsymbol{\lambda},k}^{n+1})^T$:

$$\mathbf{R}_k^{n+1} = \begin{pmatrix} \mathbf{b}_s \\ 0 \\ \mathbf{b}_f \\ R_{fs}\mathbf{b}_c|_{\Gamma^s} \end{pmatrix} - \begin{pmatrix} S(\hat{\mathbf{d}}_{s,k}^{n+1}) & - I_{\Gamma^s}^T M_{\Gamma^s} R_{sf} M_{\Gamma^f}^{-1} \boldsymbol{\lambda}_{f,k}^{n+1} \\ -R_{fs} I_{\Gamma^s} \hat{\mathbf{d}}_{s,k}^{n+1} & + G(\hat{\mathbf{d}}_{f,k}^{n+1}) \\ F(\mathbf{u}_k^{n+1}, p_k^{n+1}, \hat{\mathbf{d}}_{f,k}^{n+1}) & + I_{\Gamma^f}^T \boldsymbol{\lambda}_{f,k}^{n+1} \\ -\dfrac{\gamma}{\beta \Delta t} R_{fs} I_{\Gamma^s} \hat{\mathbf{d}}_{s,k}^{n+1} & + I_{\Gamma^f} \mathbf{u}_{f,k}^{n+1} \end{pmatrix}. \tag{4.1}$$

Then, we compute the Newton correction vector $\delta\mathbf{X}_k^{n+1} = (\delta\mathbf{d}_{s,k}^{n+1}, \delta\mathbf{d}_{f,k}^{n+1}, \delta(\mathbf{u}_k, p_k)^{n+1}, \delta\boldsymbol{\lambda}_k^{n+1})^T$ by solving

$$J_{FSI}\, \delta\mathbf{X}_k^{n+1} = -\mathbf{R}_k^{n+1}, \tag{4.2}$$

being

$$J_{FSI} = \begin{pmatrix} \mathcal{S} & 0 & 0 & -I_{\Gamma^s}^T M_{\Gamma^s} R_{sf} M_{\Gamma f}^{-1} \\ -R_{fs} I_{\Gamma^s} & \mathcal{G} & 0 & 0 \\ 0 & \mathcal{D} & \mathcal{F} & I_{\Gamma f}^T \\ -\dfrac{\gamma}{\beta \Delta t} R_{fs} I_{\Gamma^s} & 0 & I_{\Gamma f} & 0 \end{pmatrix}, \tag{4.3}$$

where $\mathcal{S}$, $\mathcal{G}$ and $\mathcal{F}$ represents the linearized structure, geometry and fluid problems, respectively; $\mathcal{D}$ are the shape derivatives (for their exact computation see [10]).

At each iteration of the Newton method, linear system (4.2) is solved by the GMRES method preconditioned by FaCSI [7]. FaCSI exploits the factorized form of the FSI Jacobian matrix, the use of static condensation to formally eliminate the interface degrees of freedom of the fluid equations, and the use of a SIMPLE preconditioner for unsteady Navier-Stokes equations. When nonconforming fluid-structure discretizations are used at the interface, the preconditioner FaCSI reads:

$$P_{FaCSI} = P_{\mathcal{S}}^{ap} \cdot P_{\mathcal{G}}^{ap} \cdot P_{\mathcal{F}}^{ap}, \tag{4.4}$$

where:

$$P_{\mathcal{S}}^{ap} = \begin{pmatrix} \mathcal{H}_{\mathcal{S}} & 0 & 0 & 0 \\ 0 & I & 0 & 0 \\ 0 & 0 & I & 0 \\ 0 & 0 & 0 & I \end{pmatrix}, \quad P_{\mathcal{G}}^{ap} = \begin{pmatrix} I & 0 & 0 & 0 \\ -R_{fs} I_{\Gamma^s} & \mathcal{H}_{\mathcal{G}} & 0 & 0 \\ 0 & 0 & I & 0 \\ 0 & 0 & 0 & I \end{pmatrix}, \tag{4.5}$$

and

$$\begin{aligned} P_{\mathcal{F}}^{ap} = {} & \begin{pmatrix} I & 0 & 0 & 0 \\ 0 & I & 0 & 0 \\ 0 & \mathcal{D} & \begin{pmatrix} I & 0 & 0 \\ 0 & I_\Gamma & 0 \\ 0 & 0 & I \end{pmatrix} & \begin{pmatrix} 0 \\ 0 \\ 0 \end{pmatrix} \\ -\frac{\gamma}{\beta \Delta t} R_{fs} I_{\Gamma^s} & 0 & \begin{pmatrix} 0 & 0 & 0 \end{pmatrix} & I \end{pmatrix} \begin{pmatrix} I & 0 & 0 & 0 \\ 0 & I & 0 & 0 \\ 0 & 0 & \begin{pmatrix} I & 0 & 0 \\ 0 & 0 & 0 \\ 0 & 0 & I \end{pmatrix} & \begin{pmatrix} 0 \\ I_\Gamma \\ 0 \end{pmatrix} \\ 0 & 0 & \begin{pmatrix} 0 & I_\Gamma & 0 \end{pmatrix} & I \end{pmatrix} \\ & \begin{pmatrix} I & 0 & 0 & 0 \\ 0 & I & 0 & 0 \\ 0 & 0 & \begin{pmatrix} \mathcal{H}_{\mathcal{K}_{ii}} & \mathcal{K}_{i\Gamma} & 0 \\ 0 & I_\Gamma & 0 \\ \mathcal{B}_i & \mathcal{B}_\Gamma & -\mathcal{H}_{\widetilde{S}} \end{pmatrix} & \begin{pmatrix} 0 \\ I_\Gamma \\ 0 \end{pmatrix} \\ 0 & 0 & \begin{pmatrix} 0 & 0 & 0 \end{pmatrix} & I \end{pmatrix} \begin{pmatrix} I & 0 & 0 & 0 \\ 0 & I & 0 & 0 \\ 0 & 0 & \begin{pmatrix} I & 0 & D^{-1}\mathcal{B}_i^T \\ 0 & I_\Gamma & 0 \\ 0 & 0 & I \end{pmatrix} & \begin{pmatrix} 0 \\ I_\Gamma \\ 0 \end{pmatrix} \\ 0 & 0 & \begin{pmatrix} 0 & 0 & 0 \end{pmatrix} & I \end{pmatrix} \\ & \begin{pmatrix} I & 0 & 0 & 0 \\ 0 & I & 0 & 0 \\ 0 & 0 & \begin{pmatrix} I & 0 & 0 \\ 0 & I_\Gamma & 0 \\ 0 & 0 & I \end{pmatrix} & \begin{pmatrix} 0 \\ 0 \\ 0 \end{pmatrix} \\ 0 & 0 & \begin{pmatrix} \mathcal{K}_{\Gamma i} & \mathcal{K}_{\Gamma\Gamma} & \mathcal{B}_\Gamma^T \end{pmatrix} & I \end{pmatrix}. \end{aligned} \tag{4.6}$$

In (4.6) we denoted by $\mathcal{K}$ and $\mathcal{B}$ the matrices representing the linearized advection-diffusion-reaction and gradient terms, respectively, split into their internal (index i) and interface (index Γ) components; furthermore, the matrix D is the diagonal of $\mathcal{K}_{ii}$.

In the preconditioner we have dropped the off-diagonal block $-I_{\Gamma^s}^T M_{\Gamma^s} R_{sf} M_{\Gamma f}^{-1}$ of J_{FSI}. In the application of FaCSI, the inverses of each diagonal, single-physics block are approximated

DOI https://doi.org/10.4208/jcm.1702-m2016-0630 | Generated on 2024-12-19 07:04:00

by efficient preconditioners denoted by $\mathcal{H}_{\mathcal{S}}$ (structure problem), $\mathcal{H}_{\mathcal{G}}$ (geometry problem), $\mathcal{H}_{\mathcal{K}_{ii}}$ and $\mathcal{H}_{\widetilde{\mathcal{S}}}$ (fluid problem) based on domain decomposition or the multigrid method. In this work we make use of the one level Algebraic Additive Schwarz (AAS) method for $\mathcal{H}_{\mathcal{S}}$, $\mathcal{H}_{\mathcal{G}}$, while the 3 level Algebraic Multigrid (AMG) method is used for $\mathcal{H}_{\mathcal{K}_{ii}}$ and $\mathcal{H}_{\widetilde{\mathcal{S}}}$. We remark that the exact local subdomain solves for AAS as well as the exact coarse solve of the AMG preconditioner are carried out by LU factorization using the library MUMPS [22, 23].

Once linear system (4.2) is solved, we update the solution, i.e. $\mathbf{X}_{k+1}^{n+1} = \mathbf{X}_{k}^{n+1} + \delta\mathbf{X}_{k}^{n+1}$. We stop the Newton iterations when $\|\mathbf{R}_{k}^{n+1}\|_{\infty}/\|\mathbf{R}_{0}^{n+1}\|_{\infty} \leq \epsilon$, being $\mathbf{R}_{0}^{n+1}$ the residual at the first Newton iteration and ϵ a prescribed tolerance.

In the fully conforming case the residual evaluation is less expensive as R_{fs}, R_{sf} and $M_{\Gamma^s} R_{sf} M_{\Gamma^f}^{-1}$ coincide with the identity matrix (in fact, using conforming discretizations, R_{sf} and R_{fs} are identity matrices and $M_{\Gamma^s} = M_{\Gamma^f}$). Indeed, in the nonconforming case to compute the residual of the structure subproblem, first we have to apply to $\boldsymbol{\lambda}_{k}^{n+1}$ the inverse of the fluid mass matrix at the interface, then interpolate it from the fluid to structure side of the interface and eventually multiply it by the interface mass matrix of the solid. The residual associated to the geometry subproblem requires to interpolate $\hat{\mathbf{d}}_{s,k}^{n+1}$ from the structure to the fluid side of the interface. The computation of $\mathbf{r}_{\boldsymbol{\lambda},k}^{n+1}$ involves interpolation of $\hat{\mathbf{d}}_{s,k}^{n+1}$ and $\mathbf{b}_c|_{\Gamma^s}$ from the structure to the fluid side of the interface.

Similarly, we notice that with respect to the conforming case, at each GMRES iteration the application of the Jacobian matrix J_{FSI} to a given input vector becomes slightly more computational expensive, too.

5. Numerical Results

Two different test cases are considered: in the first we study the fluid-structure interaction in a straight elastic tube while in the second we address the simulation of blood flow in a patient specific bypass geometry. In Section 5.1, after carrying out a mesh convergence study of the solver implemented, we report the weak and strong scalability properties of the preconditioner FaCSI in the nonconforming case and we quantify how to deal with nonconforming discretizations increases the computational costs with respect to the conforming one. In Section 5.3, we test our solver on a large-scale simulation of the hemodynamics in a femoropopliteal bypass in which both nonconforming meshes and polynomial degrees are used at the fluid-structure interface.

5.1. FSI in a straight elastic tube

The first numerical example considered is the benchmark problem proposed in [3] and numerically solved, e.g., in [1,2]. The geometry of the fluid domain consists in a straight cylinder of length $L = 5$ cm and radius $R = 0.5$ cm, surrounded by a structure with uniform thickness $t = 0.1$ cm. A normal stress of $\boldsymbol{\sigma} \cdot \mathbf{n} = 1.33 \times 10^4$ dyne/cm^2 is applied at the fluid inflow for $t \leq 0.003$ s, while a homogeneous Neumann boundary condition is used at the fluid outflow. The structure is clamped at both the ends. The fluid density and dynamic viscosity are $\rho_f = 1.0$ g/cm^3 and $\mu_f = 0.03$ g/(cm s), respectively, while the structure has density $\rho_s = 1.2$ g/cm^3, Poisson's ratio $\nu_s = 0.3$ and Young's modulus $E_s = 3 \times 10^6$ dyne/cm^2. The time step size used is $\Delta t = 10^{-4}\, s$.

5.1.1. Mesh convergence study

In this section we carry out a mesh convergence study of the solver implemented using nonconforming discretizations at the fluid-structure interface. To this end, we consider five meshes of increasing refinement: in Table 5.1 we report the information of the meshes used for the analysis. Two different types of nonconformity, identified by Set A and Set B, are taken into account.

Table 5.1: Details of the meshes used for the straight cylinder example.

	Fluid		Structure	
	# Vertices	# Tetrahedra	# Vertices	# Tetrahedra
Mesh # 1	2'337	11'040	2'460	9'600
Mesh # 2	13'603	72'000	8'052	31'680
Mesh # 3	64'943	362'400	23'028	91'200
Mesh # 4	183'300	1'045'800	60'912	272'160
Mesh # 5	285'912	1'641'180	84'816	379'440

Table 5.2: Number of Degrees of Freedom for the nonconforming polynomial degree case.

Set A - nonconforming polynomial degree				
Fluid DoF	Structure DoF	Coupling DoF	Geometry DoF	Total
9'348	48'600	2'340	7'011	67'299
54'412	159'720	7'788	40'809	262'729
259'772	458'280	22'572	194'829	935'453
733'200	1'274'616	45'036	549'900	2'602'752
1'143'648	1'775'928	58986	857'736	3'836'298

Table 5.3: Number of Degrees of Freedom (DoF) for the nonconforming meshes case.

Set B - nonconforming meshes				
Fluid DoF	Structure DoF	Coupling DoF	Geometry DoF	Total
52'152	48'600	3'160	49'815	153'727
320'338	159'720	10'472	306'735	797'265
1'568'222	458'280	30'248	1'503'279	3'560'029
4'473'327	1'274'616	60'264	4'290'027	10'098'234
6'997'815	1'775'928	84'072	6'711'903	15'569'718

In Set A, see Table 5.2, at the fluid-structure interface we use conforming meshes but nonconforming finite element dscretizations; in Set B, see Table 5.3, we address the case of nonconforming meshes. In Set A we use $\mathbb{P}1$-$\mathbb{P}1$ finite elements (stabilized by SUPG) for the fluid velocity and pressure, respectively, $\mathbb{P}2$ for the the structure displacement and $\mathbb{P}1$ for the ALE. In Set B we discretize the fluid velocity and pressure by $\mathbb{P}2$-$\mathbb{P}1$ finite elements, respectively, the structure displacement by $\mathbb{P}2$ and the ALE by $\mathbb{P}2$ as well. We point out that the nonconforming meshes used in Set B have been generated by rotating the conforming ones used in Set A such that the fluid and structure meshes overlap for roughly a third of an element length.

Let us now compare the results obtained using nonconforming discretizations with those generated in the conforming case (using more than 15 millions DoFs in total).

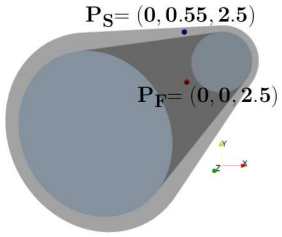

(a) Points where comparison is made.

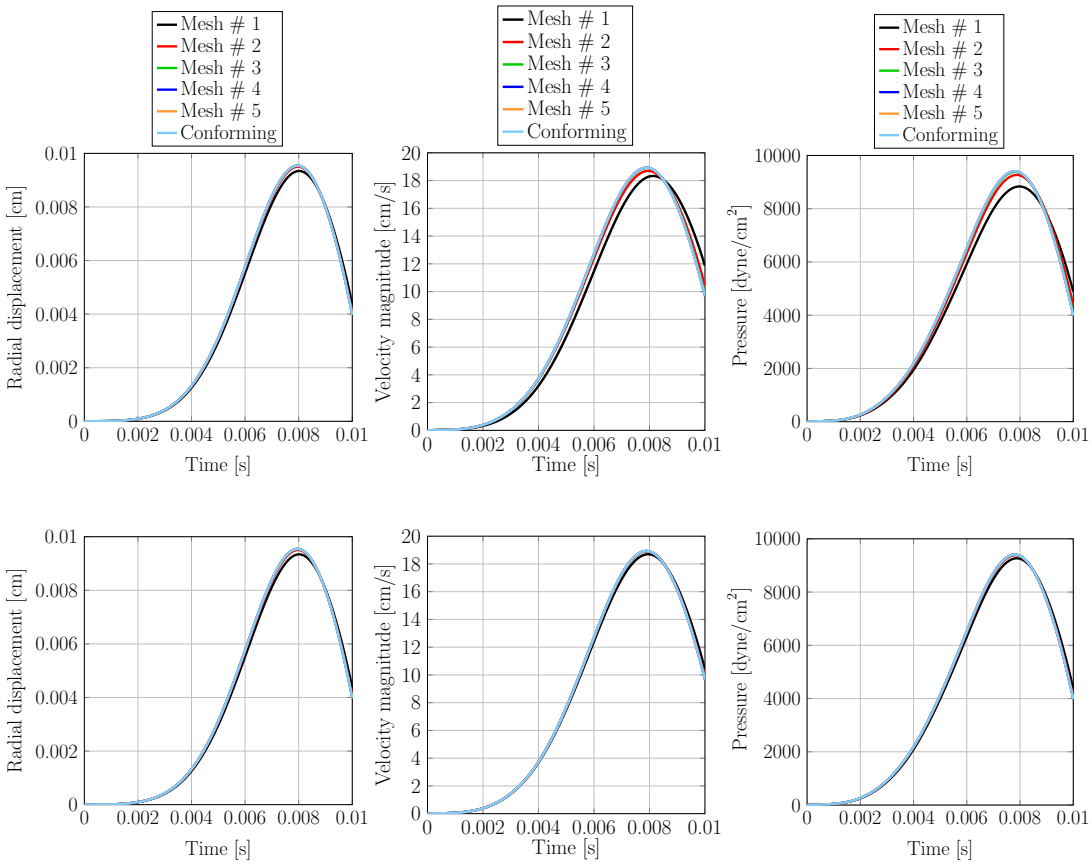

Fig. 5.1. On the top we show the locations where results are taken in the fluid ($\mathbf{P_F}$) and the structure ($\mathbf{P_S}$). From left to right we report the evolution of the radial component of the structure displacement at $\mathbf{P_S}$, the magnitude of the fluid velocity and the fluid pressure at $\mathbf{P_F}$. In the mid row we report the results for Set A while in the bottom row those generated with Set B.

In Figure 5.1 we report the solutions obtained for Set A and Set B by plotting the values of the fluid velocity and pressure, and the radial component of the solid displacements versus time at two specific locations shown in Figure 5.1(a). Furthermore, in Figure 5.2, we also report the difference between the solution obtained using conforming interface discretizations with those generated in the nonconforming case. The leftmost plots of Figure 5.1 show the mesh convergence of the structure displacements using Set A (top) and Set B (bottom). The use of quadratic finite elements in both Set A and Set B yields a very similar convergence behavior

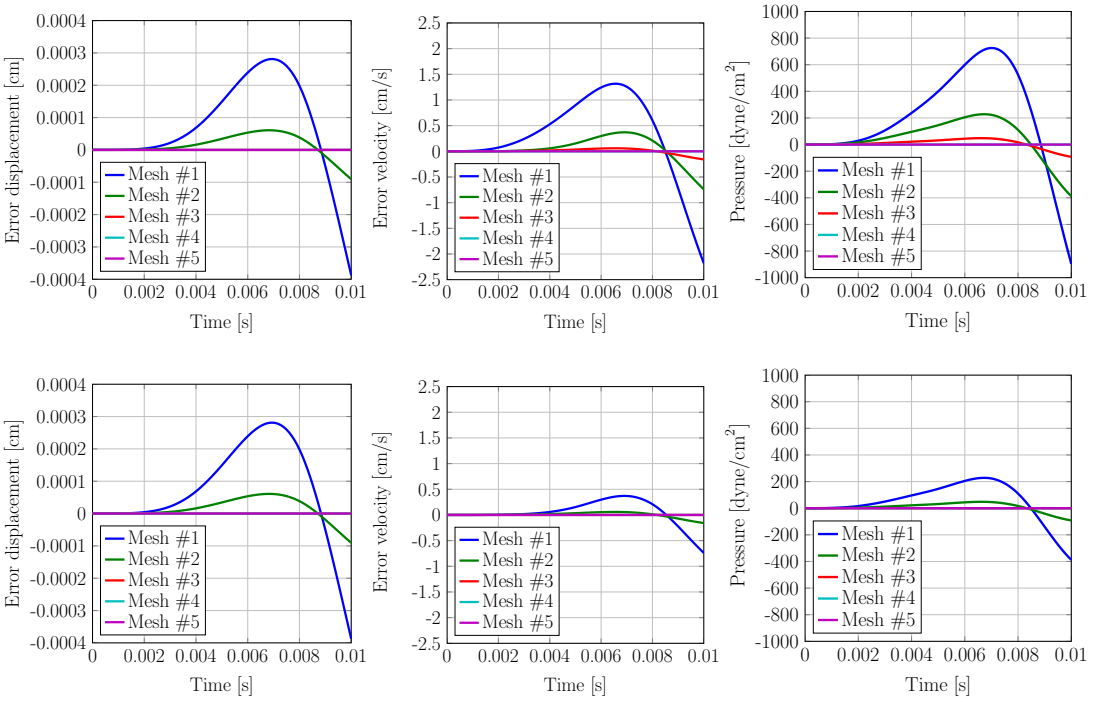

Fig. 5.2. From left to right we report the error between the solution obtained by conforming interface discretizations with those generated in the nonconforming case for the radial component of the structure displacement at $\mathbf{P_S}$, the magnitude of the fluid velocity and the fluid pressure at $\mathbf{P_F}$ (see Figure 5.1). In the top row we report the results for Set A while in the bottom row those generated with Set B.

observed in both the cases. In the middle and rightmost plots of Figure 5.1 we report the mesh convergence results for the magnitude of the fluid velocity and the fluid pressure, respectively. In this regard, we notice the different convergence behavior between Set A and Set B. Indeed, as a consequence of using $\mathbb{P}1$-$\mathbb{P}1$ elements for the fluid velocity and pressure in Set A while $\mathbb{P}2$-$\mathbb{P}1$ in Set B, the curves associated to Set B converges much faster than those of Set A.

5.2. Weak and strong scalability study of FaCSI in the nonconforming case

In this section we investigate the weak and strong scalability performance of FaCSI when nonconforming meshes are used at interface separating the fluid and structure domains. In addition, we aim at comparing the performance obtained in the nonconforming case with those reported in [7] (Section 5.1.1), where conforming fluid-structure grids were considered. For readers' convenience, in Tables 5.4 and 5.5 we report the details of the meshes adopted and the corresponding number of degrees of freedom of the discretized FSI problem. We point out that the nonconforming meshes have obtained by rotating the conforming ones.

In Figure 5.3 and 5.4 we report the weak and strong scalability results obtained, respectively (consisting in average values over the first 10 time steps simulated). For the sake of comparison, on the left column we report the weak scalability obtained in the conforming case while in the right column those with nonconforming discretizations.

By comparing the results with conforming and nonconforming fluid-structure interface discretizions, we notice that the weak scalability properties of FaCSI obtained in the nonconforming

Table 5.4: Details of the meshes used for the straight cylinder example.

	Fluid		Structure	
	# Vertices	# Tetrahedra	# Vertices	# Tetrahedra
Mesh # 1	210'090	1'202'040	65'424	292'320
Mesh # 2	559'471	3'228'960	191'080	913'920
Mesh # 3	841'341	4'880'640	300'456	1'497'600

Table 5.5: Straight flexible tube test case: number of Degrees of Freedom (DoF).

	Fluid DoF	Structure DoF	Coupling DoF	Geometry DoF	Total
Mesh # 1	5'134'050	1'369'030	195'576	4'923'960	11'622'616
Mesh # 2	13'728'971	4'119'980	456'114	13'169'500	31'474'595
Mesh # 3	20'696'341	6'599'740	598'104	19'855'000	47'749'185

case are almost the same as those using conforming meshes. In particular, the iteration count depends only mildly on both the mesh size (along each curve the number of iterations vary from roughly 22 to 36 iterations) and the number of degrees of freedom, Dofs, per core since the three curves almost overlap.

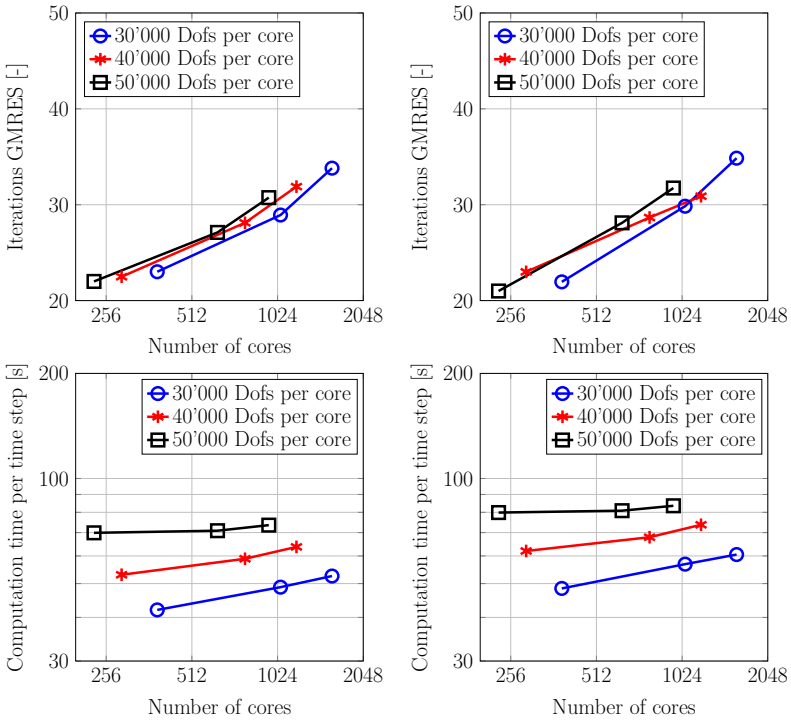

Fig. 5.3. Weak scalability results: left column with conforming discretizations, right column using nonconforming discretizations. In this study the problem size (workload) assigned to each computing core is kept constant: the different curves correspond to the results obtained using 30'000, 40'000 and 50'000 degrees of freedom per core.

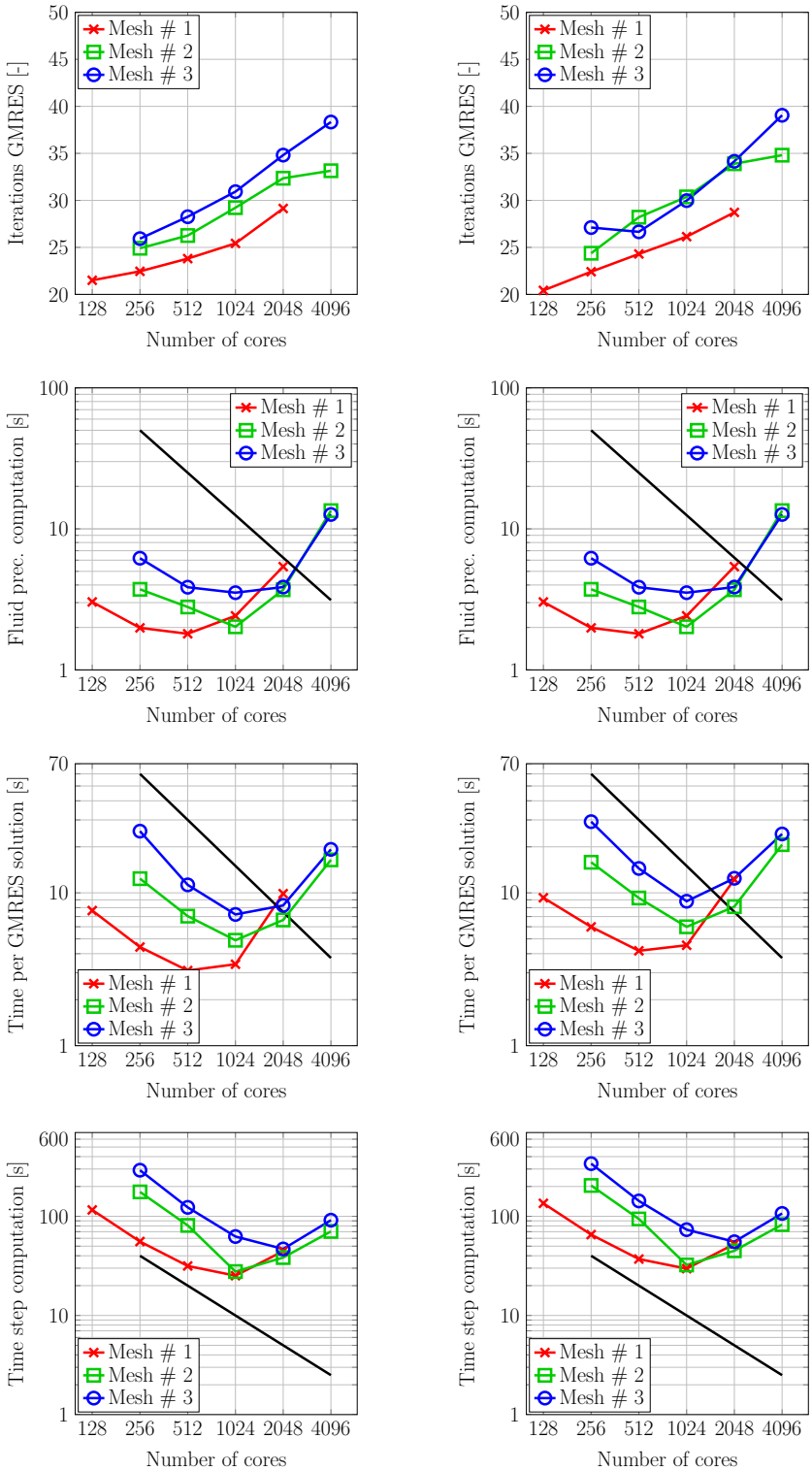

Fig. 5.4. Strong scalability results: left column with conforming discretizations, right column using non-conforming discretizations. In this study, for each of the three sets of fluid-structure meshes considered, we report the results obtained using an increasing number of computing cores.

In terms of average time to complete a single time step, we notice that it is weakly scalable for a core workload of 50'000 Dofs while for 30'000 and 40'000 it increases with the cores count as the time spent by communication is larger than the actual one associated to the relatively small amount of computational work required on each individual core.

We notice that dealing with nonconforming meshes yields an increase in computational time of approximately 15%. This is completely due, as already explained in Section 4 to the intergrid interpolations which are carried out for both the application of the exact FSI jacobian matrix and the FaCSI preconditioner at each linear solver iteration.

We focus now on the strong scalability results reported in Figure 5.4. As already observed for the weak scalability study, the strong scalabity properties of FaCSI obtained with conforming discretizations are preserved in the nonconforming case. In particular, both the iterations count and the time to build the preconditioner are very similar in both the conforming and nonconforming case. In terms of time required to solve the linear system, dealing with nonconforming FSI discretizations increases the computational costs of about 15%. Finally, we notice that the time to complete a single time step increases of about 15% too (as observed earlier in the weak scalability study) with respect to the conforming case as a consequence of the more computationally expensive solution of the linear system.

5.3. FSI in a femoropoliteal bypass

In this section we simulate the blood flow in a patient-specific femoropopliteal bypass. In this example we consider a high-resolution fluid mesh that is much finer than the one used for the structure, see Figure 5.5.

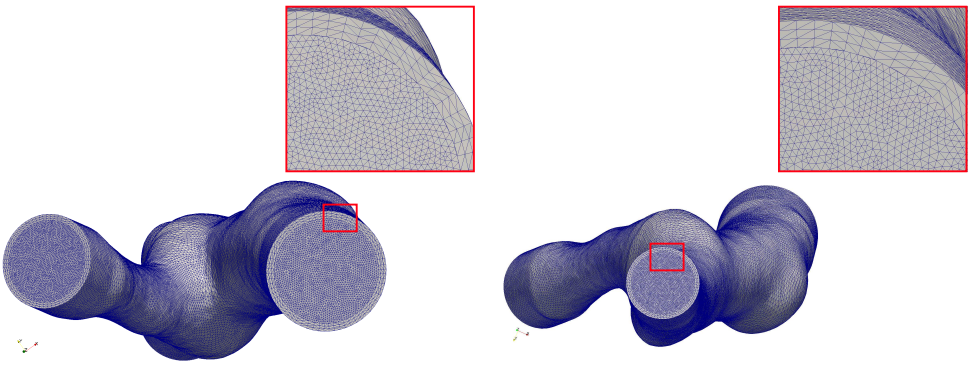

(a) Inlet Γ^f_{in} (right) and occluded branch Γ^f_{occl} (left).

(b) Outlet Γ^f_{out}.

Fig. 5.5. Meshes generated for the femoropopliteal bypass test case.

The blood is characterized by a density $\rho_f = 1\ g/cm^3$ and a dynamic viscosity $\mu_f = 0.0035\ g/(cm\,s)$. The Young's modulus of the vessel wall is $E_s = 4 \times 10^6\ dyne/cm^2$ and the Poisson's ratio is $\nu_s = 0.45$. We impose patient-specific measured flow rate on Γ^f_{in} while homogeneous Dirichlet conditions are applied at the occluded branch Γ^f_{occl}. At the outflow section of the domain Γ^f_{out} we apply a mean pressure taken from [24, Section 3.2.3], in which the same bypass geometry and inflow flow rate profile were considered. The structure is clamped at the inlets and the outlet rings where we impose $\hat{\mathbf{d}}_s = 0$. Homogenous Neumann boundary conditions are imposed at the outer surface of the vessel. We discretize the solid displacement using $\mathbb{P}2$

Table 5.6: Details of meshes used for the femoropopliteal bypass example in the nonconforming case.

Fluid		Structure	
# Vertices	# Tetrahedra	# Vertices	# Tetrahedra
2'768'791	17'247'246	113'380	508'374

Table 5.7: Number of degrees of freedom for the femoropopliteal bypass test case in the nonconforming case.

Fluid DoF	Structure DoF	Coupling DoF	Geometry DoF	Total
11'075'164	9'481'350	943'170	8'306'373	29'806'057

finite elements. For the fluid, we use $\mathbb{P}1$-$\mathbb{P}1$ elements to approximated the velocity and pressure variables (stabilized by SUPG); $\mathbb{P}1$ elements are used for the ALE map. Therefore, in this example we use both nonconforming meshes and nonconforming Finite Elements discretizations. The time step considered is $\Delta t = 0.001\ s$. In Tables 5.6 and 5.7 we report the details of the meshes used and the number of degrees of freedom, respectively.

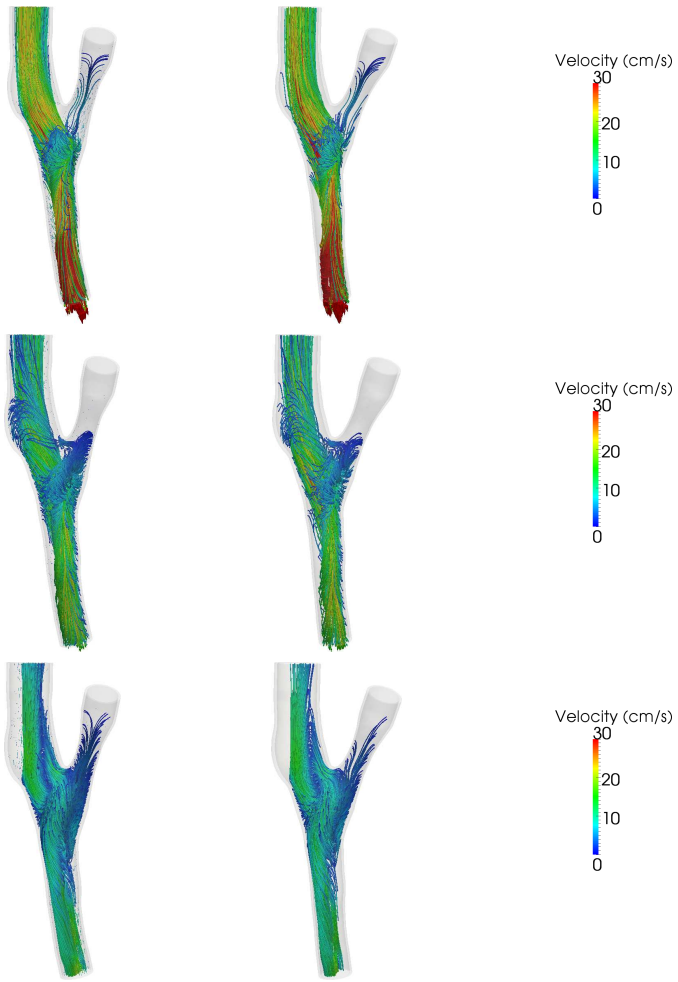

Fig. 5.6. Streamlines of the fluid flow at time $t = 1.8$ s (top), 1.9 s (middle) and 2.0 s (bottom). In the left columns we report the results obtained in the conforming case, on the right those generated using nonconforming discretizations.

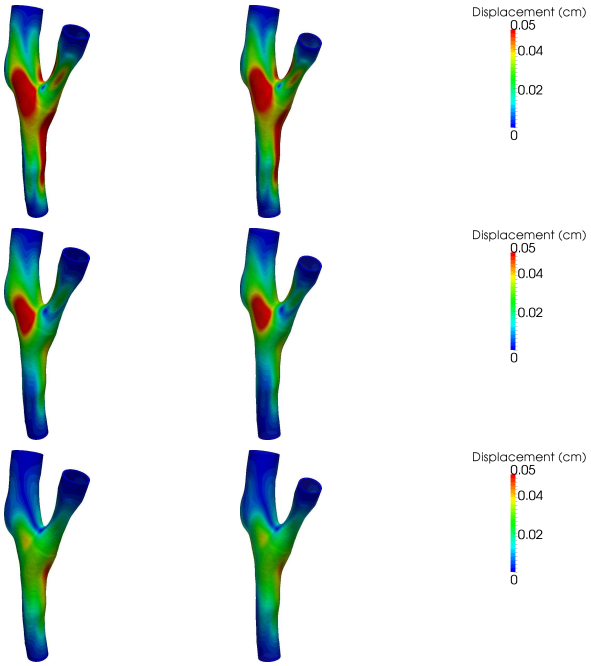

Fig. 5.7. Magnitude of the structure displacement at time $t = 1.8$ s (top), 1.9 s (middle) and 2.0 s (bottom). In the left columns we report the results obtained in the conforming case, on the right those generated using nonconforming discretizations.

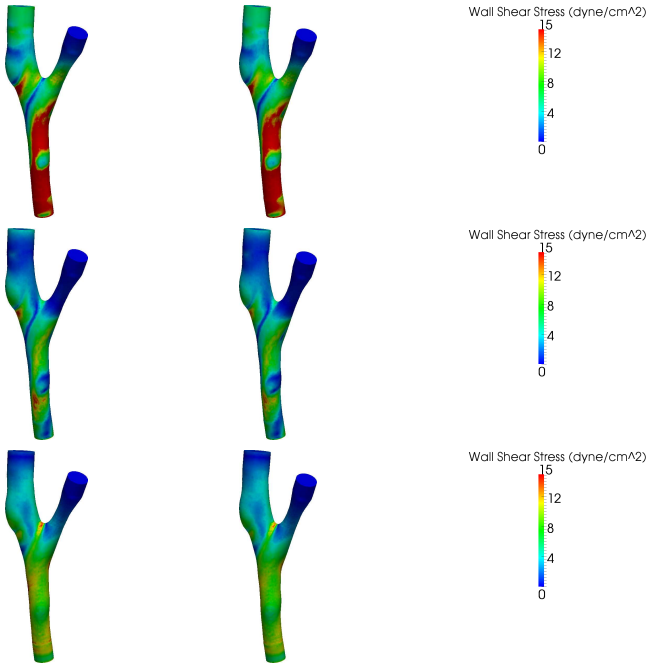

Fig. 5.8. Wall Shear Stress at time $t = 1.8$ s (top), 1.9 s (middle) and 2.0 s (bottom). In the left columns we report the results obtained in the conforming case, on the right those generated using nonconforming discretizations.

In Figures 5.6-5.8 we show the streamlines of the fluid flow, the Wall Shear Stress (WSS) distributions and the structural displacement computed at three different time steps during the third heart-beat simulated. We notice that, although nonconforming meshes and discretizations are used here, both the WSS magnitude and distribution are in good agreement with the results obtained in [7] where conforming fluid-structure meshes were adopted.

6. Conclusions

In this work we considered the numerical solution of fluid-structure interaction problems when nonconforming discretizations are used at the fluid-structure interface. In order to deal with the nonconforming discretizations we used the INTERNODES method. Furthermore, to cope with the high-resolution discretizations used in our simulations we used a parallel solver which makes use of the FaCSI preconditioner for the linearized FSI system obtained after spatial and temporal discretization. An analysis of the accuracy properties of INTERNODES applied to the FSI problem was carried out for both the case of nonconforming meshes and nonconforming polynomial degrees at the fluid-structure interface. Furthermore, we studied the strong and weak scalability properties of FaCSI and we showed that it yields almost the same performance regardless the use of conforming or nonconforming discretizations between the fluid and the structure at their interface. Finally, we used our solver developed to simulate the blood flow dynamics in a patient specific bypass geometry using both nonconforming meshes and nonconforming finite element discretizations.

Acknowledgments. The research of D. Forti was supported by the Swiss National Foundation (SNF), project no. 140184. The authors gratefully acknowledge the Swiss National Supercomputing Center (CSCS) for providing the CPU resources for the numerical simulations under project ID s635. The research of S. Deparis and A. Quarteroni was partly supported by the PASC project "Integrative HPC Framework for Coupled Cardiac Simulations".

References

[1] P. Crosetto, S. Deparis, G. Fourestey, and A. Quarteroni, Parallel algorithms for fluid-structure interaction problems in haemodynamics. *SIAM Journal on Scientific Computing*, **33**:4 (2011), 1598–1622.

[2] M.W. Gee, U. Küttler, and W.A. Wall, Truly monolithic algebraic multigrid for fluid-structure interaction. *International Journal for Numerical Methods in Engineering*, **26** (2010), 52–72.

[3] F. Nobile, *Numerical approximation of fluid-structure interaction problems with application to haemodynamics*. PhD Thesis, EPFL, 2001.

[4] Y. Bazilevs, K. Takizawa, and T. Tezduyar, *Computational Fluid–Structure Interaction. Methods and Applications*. Wiley Series in Computational Mechanics. Wiley, 2013.

[5] L. Formaggia, A. Quarteroni, and A. Veneziani, editors, *Cardiovascular mathematics*, volume 1 of *MS&A. Modeling, Simulation and Applications*. Springer-Verlag Italia, Milan. Modeling and simulation of the circulatory system, 2009.

[6] S. Deparis, D. Forti, P. Gervasio, and A. Quarteroni, INTERNODES: an accurate interpolation-based method for coupling the Galerkin solutions of PDEs on subdomains featuring non-conforming interfaces. *Computers & Fluids*, **141** (2016) 22–41.

[7] S. Deparis, D. Forti, G. Grandperrin, and A. Quarteroni, FaCSI: a block parallel preconditioner for fluid-structure interaction problems in hemodynamics. *Journal of Computational Physics*, **327** (2016), 700–718.

[8] S. Deparis, D. Forti, and A. Quarteroni, A Rescaled Localized Radial Basis Function Interpolation on Non-Cartesian and Nonconforming Grids. *SIAM Journal on Scientific Computing*, **36** (2014), A2745–A2762.

[9] S. Deparis, D. Forti, and A. Quarteroni, A fluid-structure interaction algorithm using radial basis function interpolation between non-conforming interfaces. in *Advances in Computational Fluid-Structure*, Modeling and Simulation in Science, Engineering and Technology, accepted (2015).

[10] M.A. Fernández, and M. Moubachir, An exact block-Newton algorithm for solving fluid-structure interaction problems. *C. R. Math. Acad. Sci. Paris*, **336**:8 (2003), 681–686.

[11] C. Bernardi, Y. Maday, and A.T. Patera, Domain decomposition by the mortar element method. In *Asymptotic and numerical methods for partial differential equations with critical parameters (Beaune, 1992)*, volume 384 of *NATO Adv. Sci. Inst. Ser. C Math. Phys. Sci.*, pp. 269–286. Kluwer Acad. Publ., Dordrecht, (1993).

[12] C. Bernardi, Y. Maday, and A.T. Patera, A new nonconforming approach to domain decomposition: the mortar element method. In *Nonlinear partial differential equations and their applications. Collège de France Seminar, Vol. XI (Paris, 1989–1991)*, volume 299 of *Pitman Res. Notes Math. Ser.*, pp. 13–51. Longman Sci. Tech., Harlow, (1994).

[13] F.P.T. Baaijens, A fictitious domain/mortar element method for fluid-structure interaction. *International Journal for Numerical Methods in Fluids*, **35**:7 (2001), 743–761.

[14] A. Gerstenberger, and W.A. Wall, An extended finite element method/lagrange multiplier based approach for fluid–structure interaction. *Computer Methods in Applied Mechanics and Engineering*, **197**:19 (2008), 1699–1714.

[15] T. Klöppel, A. Popp, U. Küttler, W.A. and Wall, Fluid-structure interaction for non-conforming interfaces based on a dual mortar formulation. *Computer Methods in Applied Mechanics and Engineering*, **200** (2011), 3111–3126.

[16] M. Mayr, T. Klöppel, W.A. Wall, and M.W. Gee, A temporal consistent monolithic approach to fluid-structure interaction enabling single field predictors. *SIAM Journal on Scientific Computing*, **37**:1 (2015), B30–B59.

[17] U.M. Mayer, A. Popp, A. Gerstenberger, and W.A. Wall, 3d fluidstructure-contact interaction based on a combined xfem fsi and dual mortar contact approach. *Computational Mechanics*, **46**:1 (2010), 53–67.

[18] A. Popp, M. Gitterle, M.W. Gee, and W.A. Wall, A dual mortar approach for 3d finite deformation contact with consistent linearization. *International Journal for Numerical Methods in Engineering*, **83**:11 (2010), 1428–1465.

[19] C. Farhat, M. Lesoinne, and P. Le Tallec, Load and motion transfer algorithms for fluid/structure interaction problems with non-matching discrete interfaces: Momentum and energy conservation, optimal discretization and application to aeroelasticity. *Computer Methods in Applied Mechanics and Engineering*, **157**:1 (1998), 95–114.

[20] Y.S. Cho, S. Jun, S. Im, and H.G. Kim, An improved interface element with variable nodes for non-matching finite element meshes. *Computer Methods in Applied Mechanics and Engineering*, **194**:27 (2005), 3022–3046.

[21] A. De Boer, A.H. Van Zuijlen, and H. Bijl, Review of coupling methods for non-matching meshes. *Computer Methods in Applied Mechanics and Engineering*, **196**:8 (2007), 1515–1525.

[22] P.R. Amestoy, I.S. Duff, J. Koster, and J.Y. L'Excellent, A fully asynchronous multifrontal solver using distributed dynamic scheduling. *SIAM Journal on Matrix Analysis and Applications*, **23**:1 (2001), 15–41.

[23] P.R. Amestoy, A. Guermouche, J.Y. L'Excellent, and S. Pralet, Hybrid scheduling for the parallel solution of linear systems. *Parallel Computing*, **32**:2 (2006), 136–156.

[24] C.M. Colciago, *Reduced Order Fluid-Structure Interaction Models for Hemodynamics Applications*. PhD Thesis, EPFL, Lausanne, 2014.